



OPEN ACCESS

EDITED BY

Guigen Li,
Texas Tech University, United States

REVIEWED BY

Pradeep Kumar Jaiswal,
Texas A&M University, United States
Yasmine Fernine,
Sidi Mohamed Ben Abdellah University,
Morocco
Chenyang Lu,
Purdue University, United States

*CORRESPONDENCE

Ahmed R. Rabee,
✉ ahmedrabee@alexu.edu.eg,
✉ ahmedramadanrabee@gmail.com
Mohamed Hagar,
✉ mohamedhaggar@gmail.com

RECEIVED 19 February 2025

ACCEPTED 28 April 2025

PUBLISHED 21 May 2025


CITATION

R. Rabee A, M. Soliman S, Abdel-Hamid H,
A. Moneer E, H. Akl S, H. Shahin Y, A. Masoud A,
Ghareeb DA, Jaremko M, Emwas A-H, Sherif M
and Hagar M (2025) Synthesis and
characterization of thymol-derived phenoxy
acetamide derivatives using DFT, molecular
docking, and parasitological investigations.
Front. Chem. 13:1579923.
doi: 10.3389/fchem.2025.1579923

COPYRIGHT

© 2025 R. Rabee, M. Soliman, Abdel-Hamid, A.
Moneer, H. Akl, H. Shahin, A. Masoud, Ghareeb,
Jaremko, Emwas, Sherif and Hagar. This is an
open-access article distributed under the terms
of the [Creative Commons Attribution License](#)
(CC BY). The use, distribution or reproduction in
other forums is permitted, provided the original
author(s) and the copyright owner(s) are
credited and that the original publication in this
journal is cited, in accordance with accepted
academic practice. No use, distribution or
reproduction is permitted which does not
comply with these terms.

Synthesis and characterization of thymol-derived phenoxy acetamide derivatives using DFT, molecular docking, and parasitological investigations

Ahmed R. Rabee^{1*}, Saied M. Soliman¹, Hamida Abdel-Hamid¹,
Esraa A. Moneer², Sara H. Akl², Yahya H. Shahin³,
Aliaa A. Masoud⁴, Doaa Ahmad Ghareeb ⁴, Mariusz Jaremko⁵,
Abdul-Hamid Emwas⁶, Mazen Sherif¹ and Mohamed Hagar^{1*}

¹Chemistry Department, Faculty of Science, Alexandria University, Alexandria, Egypt, ²Department of Medical Laboratory Technology, Faculty of Applied Health Sciences Technology, Pharos University in Alexandria, Alexandria, Egypt, ³Department of Medical Laboratory Technology, Faculty of Health and Medical Techniques, Almaaqal University, Basrah, Iraq, ⁴Bio-Screening and Preclinical Trial Lab, Biochemistry Department, Faculty of Science, Alexandria University, Alexandria, Egypt, ⁵Biological and Environmental Sciences and Engineering Division, King Abdullah University of Science and Technology, Makkah, Saudi Arabia, ⁶KAUST Core Laboratories, King Abdullah University of Science and Technology, Thuwal, Saudi Arabia

Novel phenoxy acetamide derivatives based on a thymol moiety were synthesized for target parasitological investigation. The newly synthesized compounds, **5a**, **5b**, **7a**, **7b**, and **9**, were synthesized as phenoxy acetamide derivatives containing a phthalimide or naphthalimide ring through a condensation reaction with various acid anhydrides. Their structures were confirmed based on spectral data derived through Fourier-transform infrared, proton and carbon-13 nuclear magnetic resonance, and elemental analyses. The parasitological, biochemical, and immunological activities of the compounds were measured. The screened compounds were subjected to molecular docking in the active site of CpCDPK1, in addition to analyses based on Lipinski's rule and SwissADME. The results showed that compounds **5a**, **5b**, and **7b** demonstrated promising antiparasitic activity, characterized by high gastrointestinal absorption and favorable drug-likeness profiles. Furthermore, **5a** and **7b** exhibited higher binding affinities than that of the reference drug. In practical assessments, compound **7b** exhibited the highest percentage reduction in oocyst counts (67%). Density functional theory calculations were performed to assess the thermodynamic stability, molecular geometry, frontier molecular orbital energy gaps, and molecular electrostatic potentials of compounds **5a**, **5b**, **7a**, **7b**, and **9**.

KEYWORDS

thymol, naphthalimide and phthalimide derivatives, anti-parasites, molecular docking, DFT

1 Introduction

Thymol (2-isopropyl-5-methylphenol) is a white crystalline aromatic compound with a distinct scent that is produced *via* the terpene pathway and typically found in the genera *Thymus* and *Origanum*. Its direct biosynthetic link with p-cymene has been demonstrated through the aromatization of c-terpinene in *Thymus vulgaris* L. (Poulose and Croteau, 1978)

According to the United States Food and Drug Administration (US-FDA), thymol is safe with low toxicity. (Cohen, 1984). Thymol has been known to exert therapeutic effects on humans, (Jyoti et al., 2019), with a range of biological activities, such as antibacterial, (Dong et al., 2024), antifungal, (Alves Eloy et al., 2021), antioxidant, (Sathe et al., 2019), antiprotozoal, (Clemente et al., 2021), anti-inflammatory, (Chen et al., 2020), antiviral, (Nandi and Khanna, 2022), antiparasitic, (Hikal et al., 2021; Sennouni et al., 2022), and anticancer (Lv and Chen, 2017; Chauhan et al., 2017) activities. Additionally, thymol has shown efficacy against *C. parvum* (*Cryptosporidium parvum*) in cell cultures. (Dominguez-Uscanga et al., 2021).

Phenoxy acetamide derivatives exhibit antioxidant activity and may protect biological systems against oxidative damage. (Al-Ostoot et al., 2021a; Arshad et al., 2022). Molecules containing acetamide linkages and their derivatives as core structures display a wide range of biological activities, (Al-Ostoot et al., 2021b), especially antitrypanosomal effects. (Capelini et al., 2021). Phthalimides, which are neutral, lipophilic compounds exhibiting antimicrobial (Akgün et al., 2012) and anti-inflammatory (Alanazi et al., 2015) properties readily penetrate biological membranes. Thus, phthalimides have been used as platforms for developing anti-*Trypanosoma cruzi* and antiplasmodial drugs. (González et al., 2014; Singh et al., 2015).

Naphthalimide derivatives have conventionally been used as fluorescent fibers and dyes. In prior decades, these derivatives were used as medicines and sensors. (Qian et al., 2010). The tricyclic planar ring structure of the naphthalimide class facilitates intercalation with DNA and disruption of biological processes. (Kamal et al., 2013). Hence, naphthalimides exhibit a range of biological attributes, such as antiviral, (Chanh et al., 1994), antioxidant, (Ghosh et al., 2015), and antimicrobial activities. (Staneva et al., 2019).

Thymol, characterized as a safe compound, (Aljohani et al., 2022), exhibits various advantages, such as abundance and low toxicity to mammalian cells. Consequently, thymol and related substances may represent promising candidates for developing novel antiparasitic therapies (Chauhan and Kang, 2014).

The zoonotic protozoan parasite *C. parvum*, which is the second-most common cause of foodborne and waterborne diarrheal illnesses globally, is a member of the phylum Apicomplexa. (Ryan et al., 2016). Its adverse effects are particularly severe for immunocompromised individuals. (Wang et al., 2018).

Considering these aspects, this study was aimed at synthesizing newly phenoxy acetamide derivatives based on a thymol moiety through condensation reactions with a series of acid anhydrides and assessing their antiparasitic effects through experimental and molecular docking studies. One of the challenges with thymol is its rapid absorption and metabolism, which can limit its effectiveness *in vivo*. The phenoxy acetamide derivatives based on thymol can potentially create prodrugs that release thymol more slowly, allowing for sustained therapeutic effects. Moreover, density functional theory (DFT) calculations were performed to explore their thermodynamic stability, molecular geometry, frontier molecular orbital (FMO) energy gaps, and molecular electrostatic potential (MEP).

2 Results and discussion

2.1 Chemistry

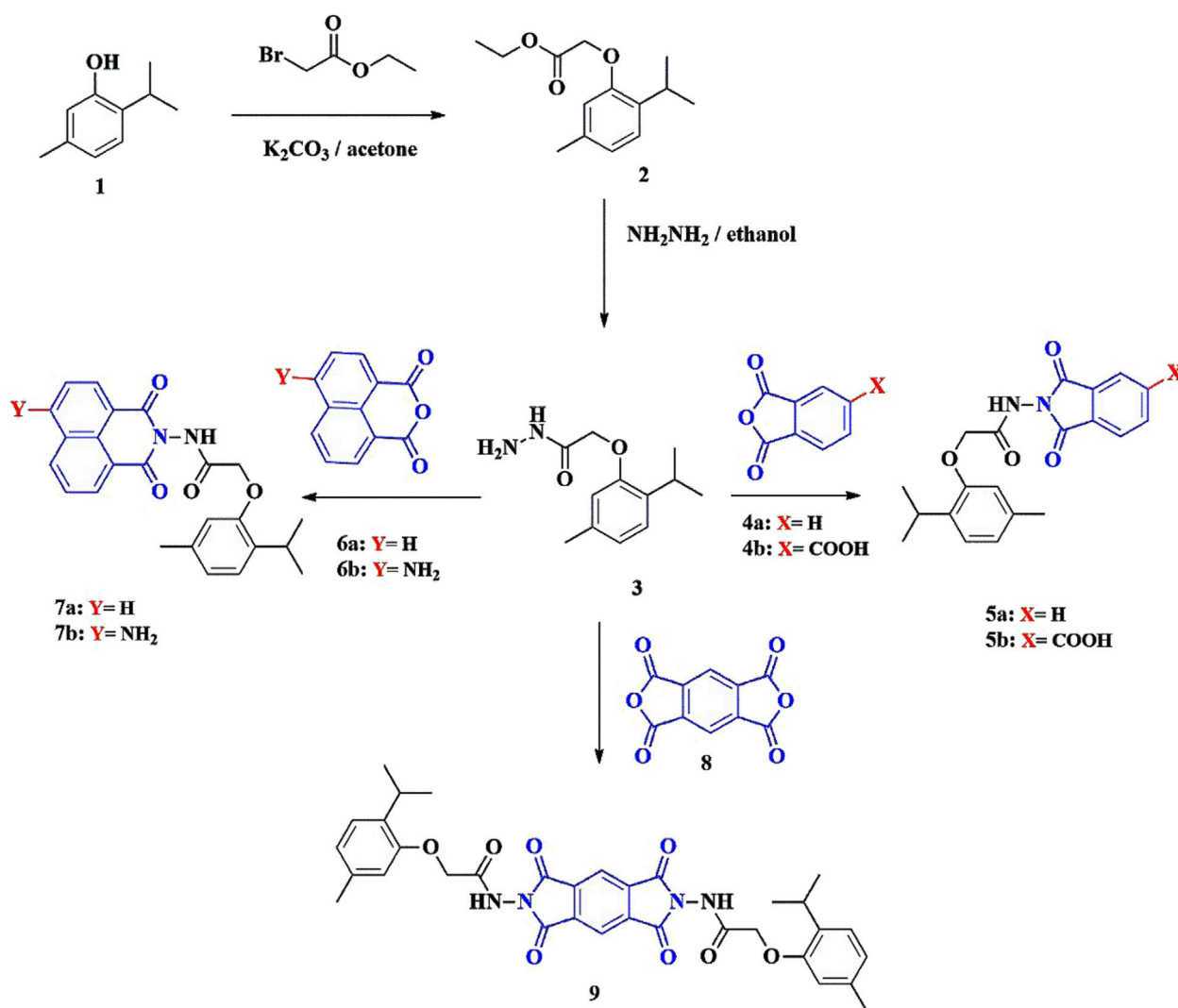
Phenoxy acetamide derivatives based on a thymol moiety were synthesized through condensation reactions with a series of acid anhydrides. As shown in Scheme 1, 2-(2-isopropyl-5-methylphenoxy)acetohydrazide (3) was reacted with different acid anhydrides, including phthalic anhydride (4a), 1,2,4-benzene tricarboxylic acid anhydride (4b), 1,8-naphthalic anhydride (6a), 4-amino-1,8-naphthalic anhydride (6b), and pyromellitic dianhydride (8) in dimethylformamide (DMF) and glacial acetic acid under reflux conditions for 4–6 h to afford compounds 5a, 5b, 7a, 7b, and 9, respectively.

The structures of the synthesized compounds 5a, 5b, 7a, 7b, and 9 were confirmed using spectroscopic data. The proton nuclear magnetic resonance (¹H-NMR) spectrum showed characteristic singlet peaks for NH (10.08–10.90 ppm) and aliphatic CH₃ (1.13–2.27 ppm). The infrared (IR) spectra of all synthesized compounds showed two sharp bands of C=O (conjugated anhydride) at $\nu = 1,792\text{ cm}^{-1}$ and $1,744\text{ cm}^{-1}$.

For compound 5b, the ¹H-NMR spectrum showed a singlet peak of COOH at 10.13 ppm and the ¹³C-NMR spectrum showed a peak at δ_c : 168.4 (COOH). The ¹H-NMR spectrum of compound 7b showed a singlet peak of NH₂ at 7.71 ppm. For compound 9, the ¹H-NMR spectrum showed two singlet peaks at 8.45 and 8.29 ppm, corresponding to pyromellitic protons.

2.2 *In silico* physicochemical and pharmacokinetic predictions

An absorption, distribution, metabolism, excretion, toxicity (ADMET) study was performed to assess the pharmacokinetic, physicochemical, and drug-likeness profiles of compounds 5a, 5b, 7a, 7b, and 9. As indicated in Table 1, compounds 5a, 5b, 7a, and 7b demonstrated high gastrointestinal (GI) absorption, whereas compound 9 exhibited low GI absorption. Blood–brain barrier (BBB) permeability was observed only for 5a and 7a. None of the compounds were substrates for P-glycoprotein. Selective inhibition of cytochrome P450 enzymes was noted, with compound 5b inhibiting CYP1A2 and compounds 5a, 7a, and 7b inhibiting CYP2C19. Furthermore, all compounds inhibited CYP2C9 and compound 9 uniquely inhibited CYP3A4. Drug-likeness analysis revealed no violations of Lipinski's rule of five for 5a, 5b, 7a, and 7b, although compound 9 exhibited two violations. Bioavailability scores were consistent for 5a, 5b, 7a, and 7b, ranging from 0.55 to 0.56, whereas compound 9 had a significantly lower score (0.17). Medicinal chemistry assessments indicated that 5b had the fewest lead-likeness violations, followed by 5a, 7a, and 7b, with compound 9 exhibiting the most violations. Synthetic accessibility scores showed that 5a was the easiest to synthesize and 9 posed the greatest challenge. Physicochemical analysis revealed that compound 9 had the highest molecular weight (626.66 g/mol) and topological polar surface area (TPSA) (154.8 Å²), correlating with low membrane permeability. Compound 5a exhibited the lowest molecular weight and TPSA, contributing to its favorable pharmacokinetic profile. Compound 9 also had the highest number of rotatable bonds, indicating greater molecular flexibility, while 5a, 7a, 7b was more rigid. Lipophilicity was most pronounced in compound 9



SCHEME 1
Synthesis of phenoxy acetamide derivatives containing a thymol unit.

(consensus log Po/w of 4.06) and **5b** exhibited the lowest value (2.54). Solubility predictions categorized **5a**, **5b**, **7a**, and **7b** as moderately soluble, while **9** was noted to be poorly soluble (ESOL log S of -6.64). Among the tested compounds, **5a**, **7a**, **7b** emerged as the most promising owing to their high GI absorption, moderate solubility (ESOL log S of -4.24 , -5.46 , -5.11), balanced lipophilicity (consensus log Po/w 2.95, 3.91, 3.39), and TPSA (75.71, 77.4, 103.42 Å²). It selectively inhibited CYP2C19 and CYP2C9 and did not interact with CYP1A2, CYP2D6, or P-gp, resulting in enhanced therapeutic safety profile. However, compound **7b** stands out as a safer candidate due to its lack of BBB permeability, which may reduce potential central nervous system side effects.

2.3 Molecular docking studies

Molecular docking results were validated by re-docking the native ligand VGG into the CDPK1 active site, considered a key target for antiparasitic drug development owing to its essential role in the lifecycle

of parasites. The analysis yielded a root mean square deviation (RMSD) of 0.52 Å and docking score of -7.27 kcal/mol, validating the proposed methodology. The binding affinity of each compound (**5a**, **5b**, **7a**, **7b**, and **9**) is outlined in Table 2. As shown in Figure 1, compound **5a** demonstrated the highest binding affinity (-7.42 kcal/mol), forming strong hydrogen bonds with critical catalytic residues Asp219, Met136 and Lys105, along with stabilizing π -alkyl and van der Waals interactions highlighting its potential as a potent inhibitor. Compound **5b** showed the second-highest binding affinity (-6.45 kcal/mol) and interacted with Asp219, Lys105, and Phe220, indicating a slightly weaker but still significant binding conformation. Compound **7b** exhibited a comparable binding affinity (-6.41 kcal/mol), with conventional hydrogen bond interactions involving Tyr155 and Asp219, suggesting a stable binding profile. In contrast, compounds **7a** and **9** displayed notably weaker binding profiles. Compound **7a** had a lower binding affinity (-5.39 kcal/mol), with limited hydrogen bond interactions involving Asp219, reflecting a less stable binding mode. Compound **9** demonstrated a highly unfavorable binding affinity (32.66 kcal/mol) owing to steric clashes and unfavorable conformations within the active

TABLE 1 ADMET study of compounds 5a, 5b, 7a, 7b, and 9.

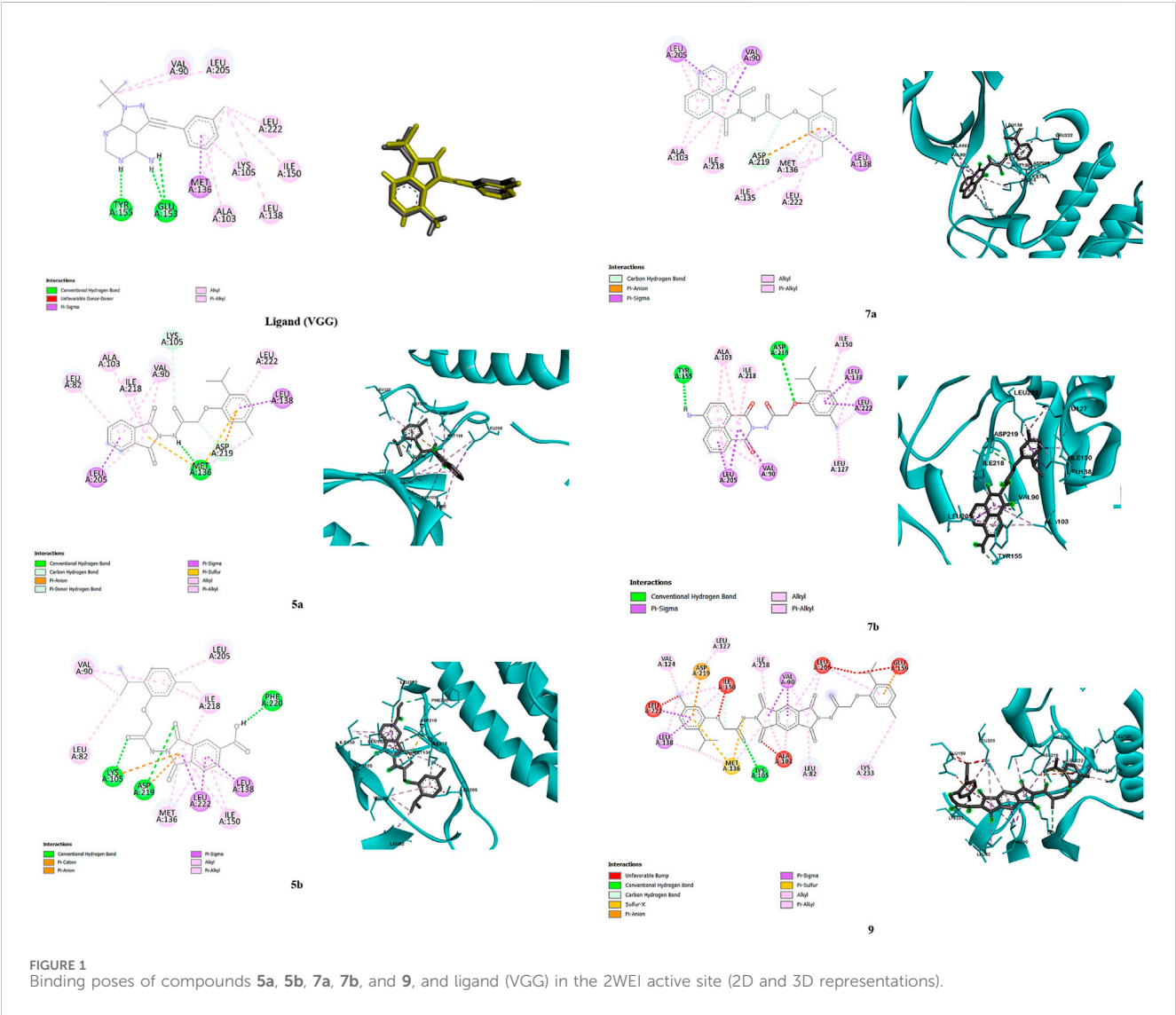
Pharmacokinetics	5a	5b	7a	7b	9
GI absorption	High	High	High	High	Low
BBB permeability	Yes	No	Yes	No	No
P-gp substrate	No	No	No	No	No
CYP1A2 inhibitor	No	Yes	No	No	No
CYP2C19 inhibitor	Yes	No	Yes	Yes	No
CYP2C9 inhibitor	Yes	Yes	Yes	Yes	Yes
CYP2D6 inhibitor	No	No	No	No	No
CYP3A4 inhibitor	No	No	No	No	Yes
Drug Likeness	5a	5b	7a	7b	9
Lipinski violations	0	0	0	0	2
Bioavailability score	0.55	0.56	0.55	0.55	0.17
Medicinal Chemistry	5a	5b	7a	7b	9
Lead likeness violations	2	1	2	2	3
Synthetic accessibility	2.75	2.98	3.08	3.19	4.27
Physicochemical Properties	5a	5b	7a	7b	9
Formula	C ₂₀ H ₂₀ N ₂ O ₄	C ₂₁ H ₂₀ N ₂ O ₆	C ₂₄ H ₂₂ N ₂ O ₄	C ₂₄ H ₂₃ N ₃ O ₄	C ₃₄ H ₃₄ N ₄ O ₈
MW	352.38	396.39	402.44	417.46	626.66
Num. heavy atoms	26	29	30	31	46
Num. aromatic heavy atoms	12	12	19	19	24
Fraction Csp ³	0.25	0.24	0.21	0.21	0.29
Num. rotatable bonds	6	7	6	6	12
Num. H-bond acceptors	4	6	4	4	8
Num. H-bond donors	1	2	1	2	2
MR	100.09	107.05	118.78	123.18	176.11
TPSA	75.71	113.01	77.4	103.42	154.8
Lipophilicity	5a	5b	7a	7b	9
Consensus log <i>P</i> _{o/w}	2.95	2.54	3.91	3.39	4.06
Water Solubility	5a	5b	7a	7b	9
ESOL log <i>S</i>	−4.24	−4.11	−5.46	−5.11	−6.64
ESOL solubility (mg/mL)	2.04E ^{−02}	3.10E ^{−02}	1.38E ^{−03}	3.22E ^{−03}	1.44E ^{−04}
ESOL solubility (mol/L)	5.78E ^{−05}	7.81E ^{−05}	3.44E ^{−06}	7.71E ^{−06}	2.29E ^{−07}
ESOL class	Moderately soluble	Moderately soluble	Moderately soluble	Moderately soluble	Poorly soluble

site, indicating a lack of inhibitory potential. Although compound **7b** had a slightly lower binding affinity than **5a** and **5b**, it demonstrated the highest *in vivo* antiparasitic activity, attributable to its balanced ADMET profile, including high GI absorption, moderate solubility, and selective cytochrome P450 inhibition, which enhanced its bioavailability and efficacy. In our *in silico* analyses, compounds **5a**, **7a**, and **7b** emerged as the most promising candidates; however, compound **7b** was particularly

notable because, in addition to its favorable ADMET properties, it selectively bound to Tyr155 in the active site which is the same residue to which the co-crystallized ligand VGG binds. This selective interaction suggests that Tyr155 plays a key role in CpCDPK1 activity, and even though **7b** exhibited slightly lower binding energy, its engagement with Tyr155 likely contributes to its enhanced antiparasitic effects. Conversely, the experimental results of compounds **7a** and **9**, which

TABLE 2 Docking scores of compounds and types of interactions with 2WEI.

Ligand compound	Binding energy score (S) (Kcal/mol)	RMSD (RefRMSD)	Inhibition constant (Ki) (μ M)	Type of binding interactions	Residues involved in the interactions
Ligand (VGG)	−7.27	0.52	4.7	Hydrogen bonds	Pyrimidine nitrogen with Tyr155, amine hydrogen with Glu153.
5a	−7.42	0.0	3.65	Hydrogen bond	Methyl hydrogen with Asp219, carbonyl oxygen with Lys105, and amide proton with Met136.
5b	−6.45	0.0	18.6	Hydrogen bond	Carbonyl oxygen with Lys105, carboxyl proton with Phe220, and carbonyl oxygen with Asp219.
7a	−5.39	0.0	111.9	Hydrogen bond	Methyl hydrogen with Asp219.
7b	−6.41	0.0	20.03	Hydrogen bond	Amine with Tyr155 and ether oxygen with Asp219
9	32.66	0.0	0.0	Unfavorable bumps	Multiple bumps



showed the lowest antiparasitic activities, correlated with their poorer docking scores and weaker binding interactions within the active site. These findings underscore the critical role of stable binding interactions, particularly with key residues, and favorable pharmacokinetic profiles in achieving potent *in vivo* activity, thereby highlighting compound 7b as a promising candidate for further drug development.

TABLE 3 *In vitro* hemolytic activity and IC₅₀ values (cytotoxicity on RBCs).

Concentration (µg/mL)	Hemolysis %				
	5a	7a	5b	7b	9
62.5	0	0	0	0	0
125	0	0	0	0	0
250	0	0	0	0	0
500	0	5.0167	0	0	0
1,000	0	6.1873	0	0	34.95
IC ₅₀ (µg/mL)	ND	6754.9	ND	ND	1,556.6

IC₅₀ (µg/mL): sample concentration causing 50% hemolysis of RBCs. ND, not determined.

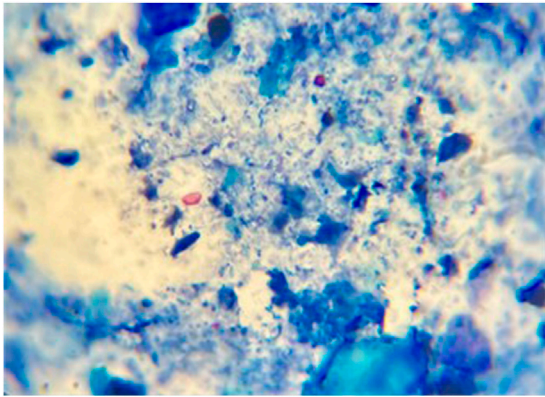


FIGURE 2
Fecal smear stained with modified Ziehl–Neelsen stain, showing *Cryptosporidium* oocysts (black arrows). Magnification: 1,000x.

2.4 Biological evaluation

2.4.1 Cytotoxic effects on red blood cells (RBCs)

The *in vitro* cytotoxic effects of the newly synthesized compounds on RBCs were assessed through hemolytic activity. The hemolysis percentages at 1,000 µg/mL were zero for **5a**, **5b**, and **7b**; 6.18% for **7a**; and 34.95% for **9** (Table 3).

2.4.2 Parasitological results

Using the modified Ziehl–Neelsen staining technique, oocysts were identified as bright-pink oval or round structures against a bluish background (Figure 2).

Table 4 indicates significant statistical differences among all groups. The mean oocyst count in the infected, non-treated group (G2) was 34.4 ± 0.69 , while the corresponding value in the nitazoxanide (NTZ)-treated group was 10.4 ± 0.51 , indicating the highest reduction in oocyst count. Among the tested compounds, the **7b**- and **7a**-treated groups exhibited the highest (67%) and lowest (51%) percentage reduction in the oocyst count, respectively.

2.4.2.1 Ultrastructural analysis

Scanning electron microscopy (SEM) was used to evaluate the ultrastructural morphological features of oocysts in fecal samples for each group. Oocysts from the control group exhibited a uniform spherical shape with smooth cyst surfaces. In contrast, cysts extracted from treated mice exhibited varying degrees of morphological changes (Figure 3).

2.4.2.2 Transmission electron microscopy (TEM)

TEM images (Figure 4) of ultrathin sections of small intestinal epithelial cells from the non-infected, non-treated control group revealed typical prominent microvilli, regular euchromatic nuclei, and well-developed cell junctions. In contrast, all treated groups revealed different levels of

TABLE 4 Number of *Cryptosporidium*-oocyst-shedding immunosuppressed mice in different study groups.

Shed oocysts/mg	G2	G3	G 4	G5	G6	G7	G8	F	P
Mean ± SD	34.4 ± 0.69	10.4 ± 0.51	13.2 ± 1.034	14.7 ± 0.67	16.8 ± 0.63	11.5 ± 0.85	15.4 ± 0.52	389.597	0.000
(R%)		70%	62%	57%	51%	67%	55%		
P within groups		P ₁ 0.000**	P ₂ 0.000**	P ₃ 0.000**	P ₄ 0.000**	P ₅ 0.000**	P ₆ 0.000**		
			P ₇ 0.004*	P ₈ 0.000**	P ₉ 0.000**	P ₁₀ 0.519 ^{ns}	P ₁₁ 0.000**		
				P ₁₂ 0.022*	P ₁₃ 0.000**	P ₁₄ 0.011*	P ₁₅ 0.002*		
					P ₁₆ 0.003*	P ₁₇ 0.000**	P ₁₈ 0.250 ^{ns}		
						P ₁₉ 0.000**	P ₂₀ 0.031*		
							P ₂₁ 0.000**		

F: One-way ANOVA, test.

P₁: G2 vs G3, P₂: G2 vs G4, P₃: G2 vs G5, P₄: G2 vs G6, P₅: G2 vs G7, P₆: G2 vs G8, P₇: G3 vs G4, P₈: G3 vs G5, P₉: G3 vs G6, P₁₀: G3 vs G7, P₁₁: G3 vs G8, P₁₂: G4 vs G5, P₁₃: G4 vs G6, P₁₄: G4 vs G7, P₁₅: G4 vs G8, P₁₆: G5 vs G6, P₁₇: G5 vs G7, P₁₈: G5 vs G8, P₁₉: G6 vs G7, P₂₀: G6 vs G8 and P₂₁: G7 vs G8.

R%: reduction percent in oocyst count.

Ns not significant, * significant at p < 0.05, ** significant at p < 0.001.

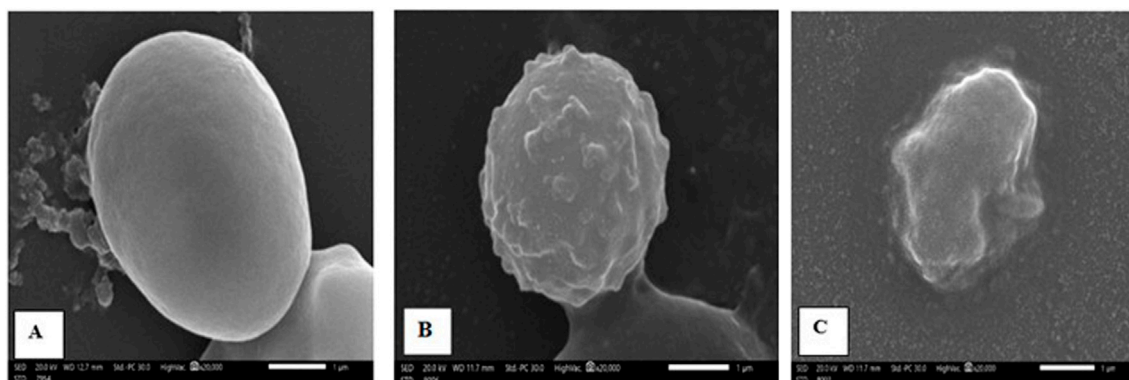


FIGURE 3
Scanning electron micrography images of *Cryptosporidium* oocysts from the (A) infected control group (G2), displaying a spherical shape with an extremely smooth surface; (B) NTZ-treated group (G3), showing rough, irregular surfaces with bleb formation; and (C) 7b-treated group, exhibiting complete distortion with irregular shapes and outlines.

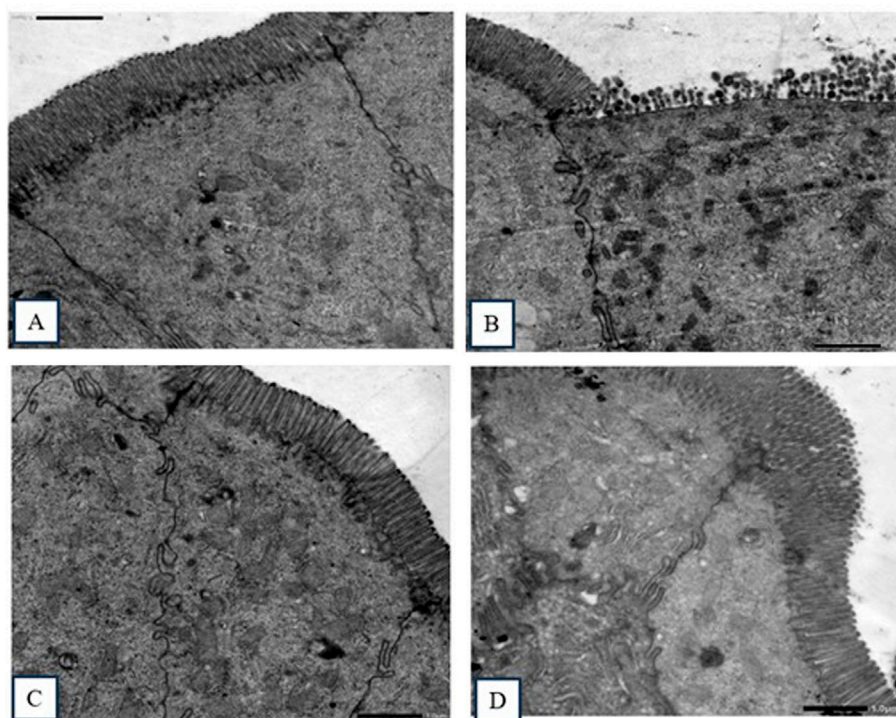


FIGURE 4
Transmission electron micrography images of sections in the small intestine. (A) Non-infected, non-treated group, showing intestinal columnar epithelial cells with normal prominent microvilli and well-developed cell junctions. (B) Infected, non-treated group, showing ileal epithelial cells with significantly damaged epithelial lining and distorted and blunted microvilli. (C) NTZ-treated group, showing normal ultrastructure and regularly arranged apical microvilli with oval euchromatic nuclei. (D) 7b-treated group, showing healthy microvilli (slightly disfigured and disarranged).

abnormalities, ranging from slight disarrangement to completely damaged atrophied microvilli.

2.4.3 Biochemical measurements

Biochemical parameter levels were significantly increased in the infected, non-treated control group compared with the negative control group. All treated groups showed significant changes in the biochemical parameter levels compared with the positive control group (Table 4).

2.4.4 Immunological measurements

In the serum cytokine analysis (Table 5), the levels of interferon-gamma (IFN- γ), tumor necrosis factor-alpha (TNF- α), interleukin-6 (IL-6), and interleukin-10 (IL-10) were significantly higher ($P < 0.001$) in the infected control group compared with the negative control group. The mean levels of IFN- γ , IL-6, and IL-10 were significantly reduced ($P < 0.001$) in the treated groups compared with the infected control group (Table 6).

TABLE 5 Cytokine levels in mice groups.

Group	TNF- α (pg/mL)	IFN- γ (pg/mL)	IL-6 (pg/mL)	IL-10 (pg/mL)
G1	9.3 \pm 0.94	342.5 \pm 4.16	88.1 \pm 0.87	253.4 \pm 1.17
G2	33.25 \pm 0.79	717.4 \pm 2.67	260.5 \pm 0.70	397.4 \pm 1.42
G3	7.8 \pm 0.91	422.1 \pm 3.21	111.4 \pm 1.17	276.5 \pm 0.97
G4	13.1 \pm 0.99	477.8 \pm 1.61	176.8 \pm 0.91	327.6 \pm 1.34
G5	13.7 \pm 1.25	494.2 \pm 3.15	181.7 \pm 1.49	387.8 \pm 0.78
G6	15.9 \pm 0.87	608.8 \pm 2.48	237.4 \pm 2.23	434.2 \pm 1.13
G7	11.8 \pm 1.03	415.2 \pm 2.57	143.1 \pm 1.1	277.2 \pm 1.47
G8	16.2 \pm 1.03	534.2 \pm 1.26	215.7 \pm 1.15	416.8 \pm 0.63
F	165.828*	1,232.828*	736.518*	1,224.031*
P	<0.001*	<0.001*	<0.001*	<0.001*

F, One-way ANOVA *P value < 0.05 significant.

TABLE 6 Biochemical analysis of mice groups.

Group	ALT (U/L)	AST (U/L)	Urea (mg/dL)	Creatinine (mg/dL)	Total protein (g/dL)	Albumin (g/dL)
G1	8.11 \pm 0.61	25 \pm 0.56	19 \pm 0.89	0.15 \pm 0.93	2.32 \pm 1.21	4.1 \pm 1.32
G2	14.35 \pm 0.63	68.32 \pm 0.85	41.42 \pm 0.98	0.69 \pm 0.39	2.62 \pm 0.96	5.16 \pm 1.11
G3	25.69 \pm 0.92	86.36 \pm 0.81	22.59 \pm 0.93	1.26 \pm 0.73	2.33 \pm 0.68	4.56 \pm 0.71
G4	24.6 \pm 1.22	97.55 \pm 0.55	26.45 \pm 0.51	1.36 \pm 0.14	2.46 \pm 0.43	4.63 \pm 0.93
G5	23.58 \pm 0.08	94.63 \pm 0.26	24.33 \pm 0.38	1.52 \pm 0.45	2.49 \pm 1.22	4.87 \pm 1.12
G6	39.68 \pm 0.82	130.5 \pm 0.67	45.34 \pm 0.36	1.76 \pm 0.36	2.4 \pm 0.62	4.8 \pm 0.84
G7	21.53 \pm 0.31	95.63 \pm 1.63	25.3 \pm 0.92	0.96 \pm 0.71	2.53 \pm 0.64	4.74 \pm 0.38
G8	30.21 \pm 0.64	105.96 \pm 0.81	35.85 \pm 0.63	1.46 \pm 0.33	2.32 \pm 0.47	4.66 \pm 0.41
F	122.815	667.930	597.905	136.462	321.651	14.631
P	<0.001*	<0.001*	<0.001*	<0.001*	<0.001*	<0.001*

F, One-way ANOVA, *P value < 0.05 significant.

2.5 DFT study

2.5.1 Geometrical structure

Compounds **5a**, **5b**, **7a**, **7b**, and **9** were theoretically examined using DFT calculations. Gauss View 6.016 (Dennington et al., 2016) was used to draw the molecular structures. Computations were performed in the gas phase using Gaussian 09 Revision D.01 software, (Caricato et al., 2009), adopting the DFT/B3LYP method at a 6–311 g basis set.

This method facilitated the optimization of the molecular geometry to determine the lowest energy and most stable structures, commonly referred to as convergence. In addition, a frequency process was applied to the optimized structures using the same basis sets to compute their thermodynamic parameters. The absence of imaginary frequencies confirmed the stability of the optimized compounds, and all synthesized compounds displayed non-coplanar structures. The optimized compounds are presented in Figure 5.

2.5.2 Polarizability and dipole moment

Molecular polarizability refers to the degree to which the electron cloud of a molecule can be distorted by an external charge, leading to the development of an electric dipole moment. (Katariya et al., 2024). The electronic nature and polarity of terminal substituents considerably affect the polarizability and dipole moment of the compound. (Soni et al., 2024). The calculated polarizability values for the investigated compounds are presented in Table 7.

Dipole moment calculations were conducted along the x, y, and z axes. It is observed that **5a** which contains only one phthalimide ring has a very low dipole moment. Meanwhile, **5b** and **7b**, have higher dipole moment values due to the presence of COOH and NH₂ groups.

2.5.3 MEP mapping

MEP mapping serves as a valuable tool for assessing electron density and charge distribution in a molecule, enabling the prediction of intermolecular and intramolecular interactions, as well as the extent of molecular packing and formal and partial charge of atoms. (Butera, 2024).

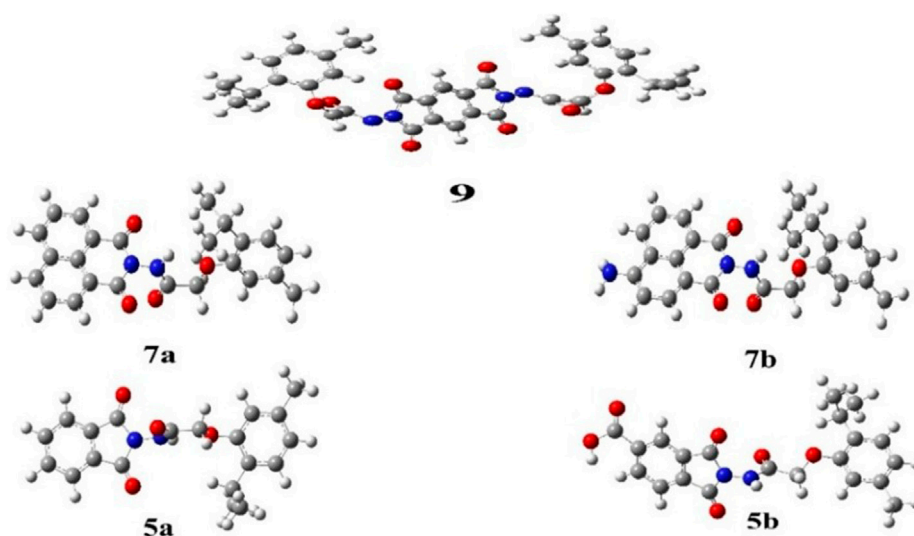


FIGURE 5
Optimized geometrical structures of synthesized phenoxy acetamide derivative compounds **5a**, **5b**, **7a**, **7b**, and **9** (gray, carbon; white, hydrogen; red, oxygen, and blue, nitrogen).

TABLE 7 Calculated polarizability (a.u.) and dipole moment (Debye) of compounds **5a**, **5b**, **7a**, **7b**, and **9**.

Compound	Dipole moment				Polarizability
	X	Y	Z	Total	
5a	-0.4286	-0.7157	-1.9086	2.0830	244.40
5b	-0.6944	-6.1862	0.1809	6.2277	265.59
7a	-3.0859	1.4869	1.3867	3.6955	295.54
7b	5.5612	0.8400	-0.9210	5.6992	310.61
9	-1.9875	3.3012	1.8926	4.2930	484.64

Following the same basis set, charge distribution maps for all compounds were derived. In the maps, regions of electron density were illustrated in ascending order: red > orange > yellow > green > blue. Specifically, regions with high electronegativity appeared in red, whereas regions with the least negative charge appeared in blue. (Politzer and Murray, 2021).

All synthesized compounds (**5a**, **5b**, **7a**, **7b**, and **9**) exhibited a high negative charge in the center regions owing to the presence of acetamide and phthalimide groups, each contributing a half-negative charge on their oxygen atoms. In compound **5b**, the highest negative charge was localized on the oxygen atom of the COOH group. The MEP maps are shown in Figure 6.

2.5.4 FMO analysis

FMOs refer to the highest occupied molecular orbital (HOMO), which donates electrons, and the lowest unoccupied molecular orbital (LUMO), which accepts electrons (Figure 7). These orbitals are essential for studying the reactivity of molecules, as they can be used to predict the electron transfer and excitation processes between orbitals based on the energy gap between HOMO and LUMO. As the energy gap widens, excitation energy rises, while reactivity falls (Tanaka, 2024).

Several physical parameters can be calculated from FMOs using the same computational method and basis sets. These parameters include the

energy gap $[(\Delta E) = (E_{\text{LUMO}} - E_{\text{HOMO}})]$, hardness $[(\eta) = (E_{\text{LUMO}} - E_{\text{HOMO}})/2]$, softness $[(S) = 1/(E_{\text{LUMO}} - E_{\text{HOMO}})]$, electronegativity $[(X) = (-E_{\text{HOMO}} - E_{\text{LUMO}})/2]$, electronic chemical potential $[(\mu) = -X]$, and fractional number of electrons transferred $[(\Delta N) = -\mu/\eta]$. The results of FMO reactivity descriptors are summarized in Table 8.

Softness indicates the sensitivity of the π -electron cloud of a molecule to potential disruptions from chemical processes. Consequently, the electronic characteristics of terminal substituents may influence softness. (Ahmed et al., 2020). For example, compounds **5b** and **9** exhibited higher softness values owing to the presence of the COOH group in **5b** and high molecular weight of compound **9**. Moreover, the electronegativity and fractional number of electrons transferred were greater in **9** than those in the other compounds, attributable to the higher electron density in this compound.

3 Materials and methods

3.1 Materials and equipment

Details regarding the materials and equipment characterization are provided in the Supplementary Material.

3.2 General procedure for condensation

A mixture containing 2-(2-isopropyl-5-methylphenoxy) acetohydrazide (**3**) (0.01 mol) and different acid anhydrides (0.01 mol), i.e., phthalic anhydride (**4a**), 1,2,4-benzene tricarboxylic acid anhydride (**4b**), 1,8-naphthalic anhydride (**6a**), 4-amino-1,8-naphthalic anhydride (**6b**), and pyromellitic dianhydride (**8**) in 15 mL DMF and a few drops of glacial acetic acid was refluxed for 4–6 h. The excess solvent was removed under reduced pressure, and the residue was poured into cold water (200 mL). The obtained solid was filtered and crystallized from ethanol to yield compounds **5a**, **5b**, **7a**, **7b**, and **9**.

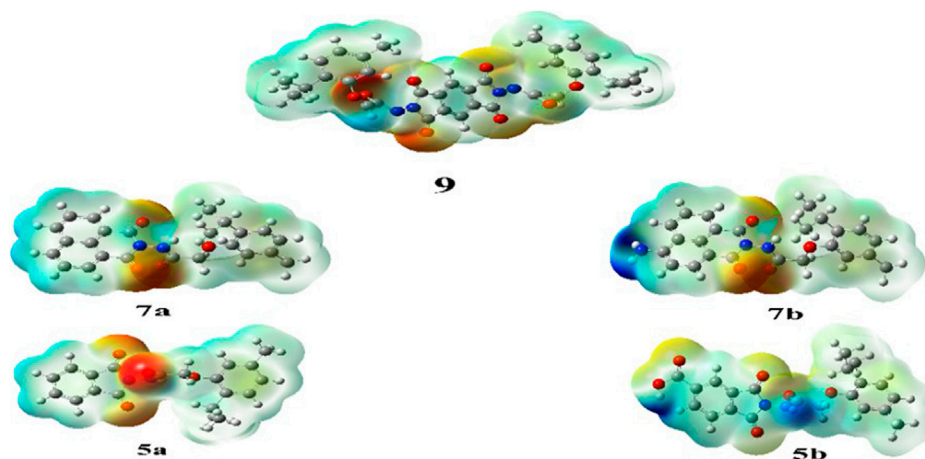


FIGURE 6
Molecular electrostatic potential (MEP) maps of synthesized compounds.

3.2.1 *N*-(1,3-dioxoisindolin-2-yl)-2-(2-isopropyl-5-methylphenoxy)acetamide (5a)

Compound **5a** as white crystals (79% yield); $R_f = 0.44$ (n-hexane: ethyl acetate, 1:2, V/V); m.p = 148°C–150°C; IR(KBr) ν_{\max} (cm⁻¹): 3427 (NH), 2955 (CH), 1792, 1744 (C=O, conjugated anhydride) observed as strong bands; ¹H-NMR (500 MHz, DMSO-*d*₆) δ_H : 10.86 (s, 1H, NH), 7.95 (d, $J = 2.5$ Hz, 2H, Ar-H), 7.91 (d, $J = 3.0$ Hz, 2H, Ar-H), 7.07 (d, $J = 7.5$ Hz, 1H, Ar-H), 6.79 (s, 1H, Ar-H), 6.75 (d, $J = 7.0$ Hz, 1H, Ar-H), 4.80 (s, 2H, CH₂), 3.23 (m, 1H, CH), 2.27 (s, 3H, CH₃), 1.13 (d, $J = 6.5$ Hz, 6H, CH₃-CH-CH₃); ¹³C-NMR (125 MHz, DMSO-*d*₆) δ_C : 168.4, 165.5, 156.3 (C=O, amide), 136.5, 135.9, 134.1, 129.9, 126.3, 124.3, 122.6, 113.7 (Ar-C), 66.8 (OCH₂), 26.2, 23.3, 21.4; Anal. calculated for C₂₀H₂₀N₂O₄: C, 68.17; H, 5.72; N, 7.95; Found: C, 67.94; H, 5.59; N, 8.02.

3.2.2 2-(2-(2-Isopropyl-5-methylphenoxy)acetamido)-1,3-dioxoisindoline-5-carboxylic acid (5b)

Compound **5b** as yellowish-white crystals (80% yield); $R_f = 0.48$ (n-hexane:ethyl acetate, 1:3, V/V); m.p = 190°C–192°C; IR(KBr) ν_{\max} (cm⁻¹): 3358 (NH), 3420 (OH), 1773, 1732 (C=O, conjugated anhydride) observed as strong bands; ¹H-NMR (500 MHz, DMSO-*d*₆) δ_H : 10.99 (bs, 1H, COOH), 10.13 (bs, 1H, NH), 8.41 (d, $J = 3.0$ Hz, 1H, Ar-H), 8.32 (d, $J = 1.5$ Hz, 1H, Ar-H), 8.07 (s, 1H, Ar-H), 7.42–6.91 (m, 1H, Ar-H), 6.74–6.28 (m, 2H, Ar-H), 4.80 (m, 2H, CH₂), 3.31 (m, 1H, CH), 2.23 (s, 3H, CH₃), 1.13 (s, 6H, CH₃-CH-CH₃); ¹³C-NMR (125 MHz, DMSO-*d*₆) δ_C : 168.4 (COOH), 167.6, 164.8, 155.4 (C=O, amide), 136.5, 136.4, 134.1, 130.3, 126.2, 126.1, 124.8, 124.3, 122.6, 122.2, 113.6, 113.4 (Ar-C), 66.8 (OCH₂), 26.2, 23.3, 21.4; Anal. calculated for C₂₁H₂₀N₂O₆: C, 63.63; H, 5.09; N, 7.07; Found: C, 63.52; H, 4.97; N, 7.19.

3.2.3 *N*-(1,3-dioxo-1*H*-benzo[*de*]isoquinolin-2(3*H*)-yl)-2-(2-isopropyl-5-methylphenoxy)acetamide (7a)

Compound **7a** as off-white crystals (82% yield); $R_f = 0.52$ (n-hexane:ethyl acetate, 1:3, V/V); m.p = 198°C–200°C; IR(KBr) ν_{\max} (cm⁻¹): 3191 (NH), 2961 (CH), 1773, 1732 (C=O, conjugated

anhydride) observed as strong bands; ¹H-NMR (500 MHz, DMSO-*d*₆) δ_H : 10.89 (s, 1H, NH), 8.52 (d, $J = 7.5$ Hz, 2H, Ar-H), 8.48 (d, $J = 7.5$ Hz, 2H, Ar-H), 7.87 (t, $J = 7.5$ Hz, 2H, Ar-H), 7.06 (d, $J = 7.5$ Hz, 1H, Ar-H), 6.90 (s, 1H, Ar-H), 6.75 (d, $J = 7.5$ Hz, 1H, Ar-H), 4.81 (s, 2H, CH₂), 3.34 (m, 1H, CH), 2.30 (s, 3H, CH₃), 1.14 (d, $J = 7.0$ Hz, 6H, CH₃-CH-CH₃); ¹³C-NMR (125 MHz, DMSO-*d*₆) δ_C : 167.8, 162.1, 155.4 (C=O, amide), 136.5, 135.9, 135.8, 134.1, 132.9, 132.1, 128.1, 127.9, 127.7, 126.2, 122.5, 122.1, 113.8 (Ar-C), 66.9 (OCH₂), 26.2, 23.3, 21.5; Anal. calculated for C₂₄H₂₂N₂O₄: C, 71.63; H, 5.51; N, 6.96; Found: C, 71.54; H, 5.42; N, 7.01.

3.2.4 *N*-(6-amino-1,3-dioxo-1*H*-benzo[*de*]isoquinolin-2(3*H*)-yl)-2-(2-isopropyl-5-methylphenoxy)acetamide (7b)

Compound **7b** as pale yellow crystals (84% yield); $R_f = 0.54$ (n-hexane:ethyl acetate, 1:3, V/V); m.p = 290°C–292°C; IR(KBr) ν_{\max} (cm⁻¹): 3436, 3350 (NH₂), 3191 (NH), 1740, 1698 (C=O, conjugated anhydride) observed as strong bands; ¹H-NMR (500 MHz, DMSO-*d*₆) δ_H : 10.09 (s, 1H, NH), 8.61 (d, $J = 8.5$ Hz, 1H, Ar-H), 8.35 (d, $J = 7.0$ Hz, 1H, Ar-H), 8.11 (d, $J = 7.5$ Hz, 1H, Ar-H), 7.71 (s, 2H, NH₂), 7.60 (t, $J = 7.0$ Hz, 1H, Ar-H), 7.01 (d, $J = 7.0$ Hz, 1H, Ar-H), 6.81 (d, $J = 7.5$ Hz, 2H, Ar-H), 6.71 (s, 1H, Ar-H), 4.54 (s, 2H, CH₂), 2.84 (m, 1H, CH), 2.19 (s, 3H, CH₃), 1.10 (s, 6H, CH₃-CH-CH₃); ¹³C-NMR (125 MHz, DMSO-*d*₆) δ_C : 162.5, 160.8, 154.4 (C=O, amide), 136.4, 134.1, 133.5, 133.0, 131.3, 131.2, 126.1, 124.8, 122.3, 119.7, 118.7, 113.4, 109.2 (Ar-C), 102.6 (CNH₂), 66.8 (OCH₂), 26.1, 23.3, 21.4; Anal. calculated for C₂₄H₂₃N₃O₄: C, 69.05; H, 5.55; N, 10.07; Found: C, 68.85; H, 5.43; N, 10.19.

3.2.5 *N,N'*-(1,3,5,7-tetraoxopyrrolo[3,4-*f*]isoindole-2,6(1*H*,3*H*,5*H*,7*H*)-diyl)bis(2-(2-isopropyl-5-methylphenoxy)acetamide) (9)

Compound **9** as yellowish-white crystals (85% yield); $R_f = 0.44$ (n-hexane:ethyl acetate, 1:3, V/V); m.p > 300°C; IR(KBr) ν_{\max} (cm⁻¹): 3358 (NH), 2962 (CH), 1744, 1715 (C=O, conjugated anhydride) observed as strong bands; ¹H-NMR (500 MHz, DMSO-*d*₆) δ_H : 11.96 (s, 1H, NH), 11.03 (s, 1H, NH), 8.45

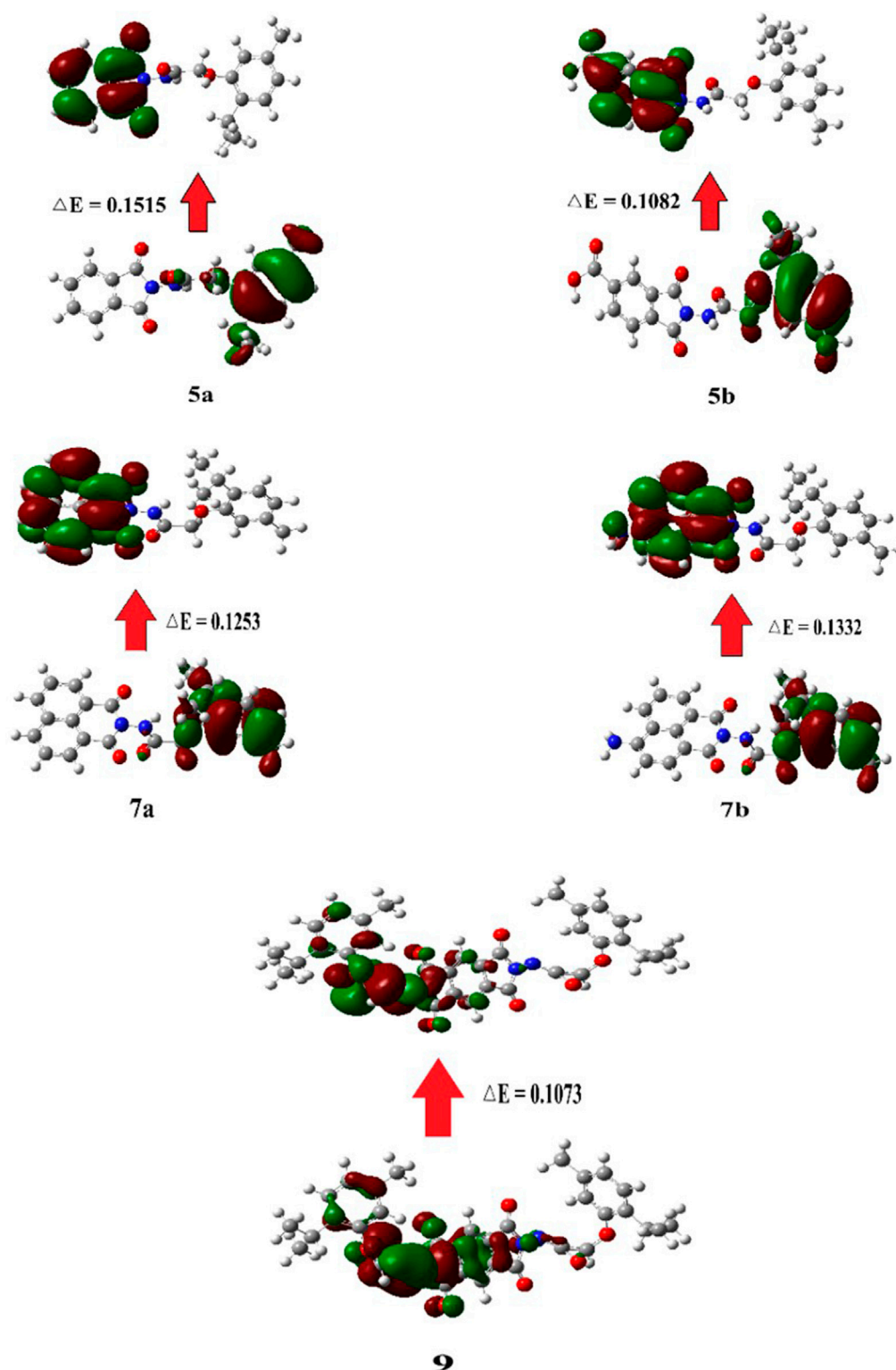


FIGURE 7
Graphical representation of the frontier molecular orbitals (FMOs) of compounds 5a, 5b, 7a, 7b, and 9.

(s, 1H, pyromellitic-H), 8.29 (s, 1H, pyromellitic-H), 7.07–6.59 (m, 6H, Ar-H), 4.82 (s, 4H, 2CH₂), 3.07 (m, 2H, 2CH), 2.27 (s, 6H, 2CH₃), 1.13 (d, $J = 6.5$ Hz, 12H, 2CH₃-CH-CH₃); ¹³C-NMR (125 MHz, DMSO-*d*₆) δ_C : 168.3, 166.8, 163.9, 163.8, 155.2 (C=O,

amide), 138.4, 136.5, 135.7, 135.6, 134.9, 134.1, 126.3, 122.6, 119.7, 118.5, 118.4, 113.6, 113.5 (Ar-C), 66.7, 66.6 (OCH₂), 26.3, 24.8, 23.3, 23.2, 21.5, 21.3; Anal. calculated for C₃₄H₃₄N₄O₈: C, 65.17; H, 5.47; N, 8.94; Found: C, 65.02; H, 5.34; N, 9.01.

TABLE 8 FMO energies (eV), energy difference (eV), and corresponding parameters of investigated compounds.

Compound	E _{HOMO}	E _{LUMO}	ΔE	η	S = 1/η	χ	μ = -χ	ΔN = -μ/η
5a	-0.2423	-0.0909	0.1515	0.0757	13.2031	0.1666	-0.1666	2.1995
5b	-0.2239	-0.1157	0.1082	0.0541	18.4860	0.1698	-0.1698	3.1381
7a	-0.2260	-0.1008	0.1253	0.0626	15.9681	0.1634	-0.1634	2.6094
7b	-0.2232	-0.0900	0.1332	0.0666	15.0161	0.1566	-0.1566	2.3519
9	-0.2329	-0.1256	0.1073	0.0537	18.6393	0.1793	-0.1793	3.3418

3.3 *In silico* physicochemical and pharmacokinetic predictions

The method of ADMET study is provided in the [Supplementary Material](#).

3.4 *In silico* molecular docking

The method of *In silico* Molecular Docking study is provided in the [Supplementary Material](#).

3.5 Biological evaluation

3.5.1 Hemolytic activity assay

The hemolytic effect of different compounds was evaluated using an existing method. (Diaconu et al., 2020). One milliliter of rat blood was collected, added to a sterile, screw-top EDTA tube, and centrifuged at 3000 rpm for 20 min. The upper layer was decanted, and the erythrocytes were rinsed several times with 10 mL of cooled isotonic and sterile phosphate-buffered saline (PBS) with a pH of 7.4. The rinsed cells were re-suspended in 20 mL sterile, cold PBS. The compounds (serial dilutions of 62.5–1,000 µg/mL in DMSO) were added to the erythrocyte solution and incubated for 60 min at 37°C. After centrifugation at 3000 rpm for 10 min, the absorbance of hemoglobin in the supernatant at 540 nm was used to calculate the hemolysis rate. Triton X-100 (0.1% in PBS) was used as a positive control, and the vehicle (PBS/DMSO) was used as the negative control. The hemolysis percentage was calculated as follows: Hemolysis percentage = (Ab of sample – Ab of negative control)/(Ab of positive control–Ab of negative control) × 100.

3.5.2 Drugs

NTZ was orally administered as a reference drug at a dose of 250 mg/kg/d for 10 successive days, starting from the 7th day of infection. (Fahmy et al., 2021).

3.5.3 Preparation of *Cryptosporidium* oocysts

Cryptosporidium oocysts were obtained from the Parasitology Lab, Theodor Bilharz Research Institute, Giza, Egypt. Before infection, the oocysts were concentrated and counted in PBS using a hemocytometer. To maintain the organism cycle, five mice were inoculated with 3000–3500 oocysts using a tuberculin syringe in an intra-esophageal manner. (Operario et al., 2015).

3.5.4 Experimental animals

Eighty healthy laboratory-bred adult male Swiss albino mice weighing 30–40 g were purchased from the animal house of the Faculty of Pharmacy, Pharos University. The animals were allowed to acclimatize for 1 week to the environmental conditions and housed in grouped plastic cages away from direct sunlight, under appropriate sanitary conditions and controlled temperature and humidity.

3.5.5 Immunosuppression

Immune suppression was induced and maintained throughout the experiment by administering dexamethasone (Dexazone, Al Kahira Pharmaceutical and Chemical Industries) through oral-gastric gavage at a dose of 0.25 mg/g/d for 14 consecutive days prior to inoculation with *Cryptosporidium* oocysts. (Najoom et al., 2021).

3.5.6 Infection

On day 15 of dexamethasone treatment, mice in the infected groups were inoculated with 10⁴ *Cryptosporidium* oocysts using oral-gastric gavage. Before infection, oocysts were concentrated and counted in PBS using a hemocytometer.

3.5.7 Study design

Mice were distributed equally into eight groups of 10 each. At the end of the experiment, all animals were anesthetized for parasitological, ultrastructural, immunological, and biochemical studies. Mice grouping details are provided in the [Supplementary Material](#).

3.5.8 Parasitological examination

On the final day of the experiment (30 days post infection), fresh fecal pellets from the infected mice in each group were collected to count the number of oocysts. Every sample was homogenized through suspension in double-distilled H₂O. Subsequently, a fecal smear of 1 mg feces was prepared and stained using the modified Ziehl–Neelsen staining method. The stained fecal smear was examined microscopically, and the *Cryptosporidium* oocysts were counted. The number of oocysts per mg feces for each mouse was tabulated as the mean value for each group. All reported data represent the means of three independent trials.

3.5.9 Ultrastructural analysis

3.5.9.1 SEM

Fecal samples from each group were harvested in a 2.5% glutaraldehyde solution and examined using a scanning electron

microscope (Hassan et al., 2023) to detect morphological changes. An aliquot (20 μ L) of dispersed flow cell biofilm sample was fixed in an equal volume of 5.0% glutaraldehyde in sterile 1 \times PBS. The samples were immobilized and attached to 0.01% poly-L-lysine (Sigma, USA) coated round coverslips (12 mm) and subjected to high-resolution imaging using an in-lens secondary electron detector at an accelerating voltage of 3 kV (Zeiss 55 VP field-emission SEM).

3.5.9.2 TEM

The small intestine of each mouse was removed, cut into small pieces (1 mm³), fixed in 2% glutaraldehyde in 0.1 M phosphate buffer, postfixed in 1% osmium tetroxide for 2 h at 4°C, dehydrated, and embedded in Epon. Semi-thin and ultrathin sections (two samples per mouse) were prepared using an ultramicrotome. The sections were stained and analyzed using a transmission electron microscope.

3.5.9.3 Biochemical measurements

Blood samples were collected from each group, transferred into tubes, and centrifuged at 3000 rpm for 5 min. The clear, non-hemolyzed supernatant serum was separated into clean tubes and stored at –20°C until use. Alanine aminotransferase (ALT) and aspartate aminotransferase (AST) levels were determined using commercially available spectrophotometric diagnostic kits (Sigma-Aldrich) according to the manufacturer instructions.

3.5.9.4 Immunological measurements

Serum concentrations of IFN- γ , TNF- α , IL-6, and IL-10 for each group were determined using an enzyme-linked immunosorbent assay reader, following the manufacturer's protocol.

3.5.9.5 Statistical analysis

The results were calculated, tabulated, and statistically analyzed using the statistical computer program SPSS version 24 (Windows 10). Data were expressed as mean \pm standard deviation (SD). Differences between groups were determined using a one-way analysis of variance (ANOVA) to compare one variable across groups. The level of significance was defined as $P < 0.05$.

3.5.9.6 Ethics approval

The experiments were performed in accordance with the guidelines of the Institutional Animal Care and Use Committee (IACUC) at the Faculty of Medicine, Alexandria University (AU 04/24/12/30/3/03) as well as the Animal Research: Reporting of *In Vivo* Experiments (ARRIVE) guidelines. The mice anesthetized through intraperitoneal injections of ketamine hydrochloride (100 mg/kg) and xylazine (10 mg/kg).

compound **7b** exhibiting the highest percentage reduction (67%). Moreover, all treated groups showed significant changes in the biochemical parameter levels compared with the positive control group. The mean serum levels of INF- γ , IL-6, and IL-10 were significantly reduced in all treated groups compared with the infected control group. DFT calculations indicated that compounds **5a**, **5b**, and **7b** exhibited a high energy gap between FMOs and high dipole moment values, which may be strongly correlated with their bioactivity. Therefore, compounds **5a**, **5b**, and **7b** represent promising candidates for the development of efficient antiparasitic drugs.

Data availability statement

The raw data supporting the conclusions of this article will be made available by the authors, without undue reservation.

Ethics statement

The present experiment was performed in accordance with the Animal Care and Use Committee at the Faculty of Medicine (Institutional Animal Care and Use Committee (IACUC) Alexandria University (AU 04/24/12/30/3/03). The study was conducted in accordance with the local legislation and institutional requirements.

Author contributions

AR: Methodology, Writing – original draft, Writing – review and editing. SM: Supervision, Writing – review and editing, Validation. HA-H: Supervision, Writing – review and editing. EA: Investigation, Writing – review and editing. SH: Investigation, Writing – review and editing. YH: Data curation, Writing – review and editing. AA: Formal Analysis, Writing – review and editing. DG: Data curation, Writing – review and editing. MJ: Funding acquisition, Writing – review and editing. A-HE: Funding acquisition, Writing – review and editing. MS: Software, Writing – review and editing. MH: Writing – original draft.

Funding

The author(s) declare that financial support was received for the research and/or publication of this article. Open access funding provided by The Science, Technology & Innovation Funding Authority (STDF) in cooperation with The Egyptian Knowledge Bank (EKB) with (ID 46267).

5 Conclusion

This study reports the design and synthesis of novel phenoxy acetamide derivatives (**5a**, **5b**, **7a**, **7b**, and **9**) based on a thymol moiety for target parasitological treatments. All synthesized compounds demonstrated a reduction in oocyst counts, with

Conflict of interest

The authors declare that the research was conducted in the absence of any commercial or financial relationships that could be construed as a potential conflict of interest.

Generative AI statement

The author(s) declare that no Generative AI was used in the creation of this manuscript.

Publisher's note

All claims expressed in this article are solely those of the authors and do not necessarily represent those of their affiliated organizations,

or those of the publisher, the editors and the reviewers. Any product that may be evaluated in this article, or claim that may be made by its manufacturer, is not guaranteed or endorsed by the publisher.

Supplementary material

The Supplementary Material for this article can be found online at: <https://www.frontiersin.org/articles/10.3389/fchem.2025.1579923/full#supplementary-material>

References

- Ahmed, N. H., Saad, G. R., Ahmed, H. A., and Hagar, M. (2020). New wide-stability four-ring azo/ester/Schiff base liquid crystals: synthesis, mesomorphic, photophysical, and DFT approaches. *RSC Adv.* 10, 9643–9656. doi:10.1039/c9ra10499b
- Akgün, H., Karamlekoglu, İ., Berk, B., Kurnaz, I., Sarıbiyık, G., Öktem, S., et al. (2012). Synthesis and antimycobacterial activity of some phthalimide derivatives. *Bioorg. & Med. Chem.* 20, 4149–4154. doi:10.1016/j.bmc.2012.04.060
- Alanazi, A. M., El-Azab, A. S., Al-Suwaidan, I. A., ElTahir, K. E. H., Asiri, Y. A., Abdel-Aziz, N. I., et al. (2015). Structure-based design of phthalimide derivatives as potential cyclooxygenase-2 (COX-2) inhibitors: anti-inflammatory and analgesic activities. *Eur. J. Med. Chem.* 92, 115–123. doi:10.1016/j.ejmech.2014.12.039
- Aljohani, F. S., Rezki, N., Aouad, M. R., Elwakil, B. H., Hagar, M., Sheta, E., et al. (2022). Synthesis, characterization and nanoformulation of novel sulfonamide-1, 2, 3-triazole molecular conjugates as potent antiparasitic agents. *Int. J. Mol. Sci.* 23, 4241. doi:10.3390/ijms23084241
- Al-Ostoot, F. H., Sherapura, A., V. V., Basappa, G., Hk, V., Bt, P., et al. (2021a). Targeting HIF-1 α by newly synthesized Indolephenoxyacetamide (IPA) analogs to induce anti-angiogenesis-mediated solid tumor suppression. *Pharmacol. Rep.* 73, 1328–1343. doi:10.1007/s43440-021-00266-8
- Al-Ostoot, F. H., Zabiulla, M., Salah, S., and Khanum, S. A. (2021b). Recent investigations into synthesis and pharmacological activities of phenoxy acetamide and its derivatives (chalcone, indole and quinoline) as possible therapeutic candidates. *J. Iran. Chem. Soc.* 18, 1839–1875. doi:10.1007/s13738-021-02172-5
- Alves Eloy, M., Ribeiro, R., Martins Meireles, L., Antonio de Sousa Cutrim, T., Santana Francisco, C., Lirian Javarini, C., et al. (2021). Thymol as an interesting building block for promising fungicides against *Fusarium solani*. *J. Agric. Food Chem.* 69, 6958–6967. doi:10.1021/acs.jafc.0c07439
- Arshad, M. F., Alam, A., Alshammari, A. A., Alhazza, M. B., Alzimam, I. M., Alam, M. A., et al. (2022). Thiazole: a versatile standalone moiety contributing to the development of various drugs and biologically active agents. *Molecules* 27, 3994. doi:10.3390/molecules27133994
- Butera, V. (2024). Density functional theory methods applied to homogeneous and heterogeneous catalysis: a short review and a practical user guide. *Phys. Chem. Chem. Phys.* 26, 7950–7970. doi:10.1039/d4cp00266k
- Capelini, C., de Souza, K. R., Barbosa, J. M., Salomão, K., Sales Junior, P. A., Murta, S. M., et al. (2021). Phenoxycetohydrazones against *Trypanosoma cruzi*. *Med. Chem. Res.* 30, 1703–1712. doi:10.1007/s00044-021-02768-9
- Caricato, M., Frisch, M. J., Hiscoks, J., and Frisch, M. J. (2009). *Gaussian 09: IOPs reference*. CT, USA: Gaussian Wallingford.
- Chanh, T. C., Lewis, D. E., Judy, M. M., Sogandares-Bernal, F., Michalek, G. R., Utech, R. E., et al. (1994). Inhibition of retrovirus-induced syncytium formation by photoproducts of a brominated 1,8-naphthalimide compound. *Antivir. Res.* 25, 133–146. doi:10.1016/0166-3542(94)90102-3
- Chauhan, A. K., Bahuguna, A., Paul, S., and Kang, S. C. (2017). Thymol elicits HCT-116 colorectal carcinoma cell death through induction of oxidative stress. *Anti-Cancer Agents Med. Chem. Former. Curr. Med. Chemistry-Anti-Cancer Agents* 17, 1942–1950. doi:10.2174/1871520617666170327121228
- Chauhan, A. K., and Kang, S. C. (2014). Thymol disrupts the membrane integrity of *Salmonella* ser. typhimurium *in vitro* and recovers infected macrophages from oxidative stress in an *ex vivo* model. *Res. Microbiol.* 165, 559–565. doi:10.1016/j.resmic.2014.07.001
- Chen, J., Li, D.-L., Xie, L.-N., Ma, Y.-r., Wu, P.-P., Li, C., et al. (2020). Synergistic anti-inflammatory effects of silibinin and thymol combination on LPS-induced RAW264.7 cells by inhibition of NF- κ B and MAPK activation. *Phytomedicine* 78, 153309. doi:10.1016/j.phymed.2020.153309
- Clemente, C. M., Ravetti, S., Allemandi, D. A., Hergert, L. Y., Pineda, T., and Robledo, S. M. (2021). Synthesis, *in vitro* antiprotozoal activity and cytotoxicity of new thymol carbonate derivatives. *ChemistrySelect* 6, 6597–6600. doi:10.1002/slct.202101461
- Cohen, S. (1984). *US Environmental Protection Agency, office of pesticide programs*. Pomerantz (Environmental Prot. Agency, Off, 5–13).
- Dennington, R., Keith, T. A., and Millam, J. M. (2016). *GaussView, version 6.0*. 16. Semichem Inc Shawnee Mission KS.
- Diaconu, M., Pavel, L. V., Hlihor, R.-M., Rosca, M., Fertu, D. I., Lenz, M., et al. (2020). Characterization of heavy metal toxicity in some plants and microorganisms—a preliminary approach for environmental bioremediation. *New Biotechnol.* 56, 130–139. doi:10.1016/j.nbt.2020.01.003
- Dominguez-Uscanga, A., Aycart, D. F., Li, K., Witola, W. H., and Laborde, J. E. A. (2021). Anti-protozoal activity of Thymol and a Thymol ester against *Cryptosporidium parvum* in cell culture. *Int. J. Parasitol. Drugs Drug Resist.* 15, 126–133. doi:10.1016/j.ijpddr.2021.02.003
- Dong, H., You, Y., Wang, N., Wang, M., Song, T., He, Y., et al. (2024). Development of amphipathic derivatives of thymol and carvacrol as potent broad-spectrum antibacterial agents. *Eur. J. Med. Chem.* 276, 116716. doi:10.1016/j.ejmech.2024.116716
- Fahmy, M.-E. A., Abdelaal, A. A., Hassan, S. I., Shalaby, M. A., Ismail, M. A. M., Khairy, R. A., et al. (2021). Antiparasitic and immunomodulating effects of nitazoxanide, ivermectin and selenium on *Cryptosporidium* infection in diabetic mice. *Rev. Bras. Parasitol. Veterinária* 30, e012121. doi:10.1590/s1984-29612021087
- Ghosh, P., Singha Roy, S., Basu, A., Bhattacharjee, A., and Bhattacharya, S. (2015). Sensitization of cisplatin therapy by a naphthalimide based organoselenium compound through modulation of antioxidant enzymes and p53 mediated apoptosis. *Free Radic. Res.* 49, 453–471. doi:10.3109/10715762.2015.1012079
- González, M. A., Clark, J., Connelly, M., and Rivas, F. (2014). Antimalarial activity of abietane ferruginol analogues possessing a phthalimide group. *Bioorg. & Med. Chem. Lett.* 24, 5234–5237. doi:10.1016/j.bmcl.2014.09.061
- Hassan, E. M., Soliman, S. M., Moneer, E. A., Hagar, M., Barakat, A., Haukka, M., et al. (2023). Synthesis, X-ray structure, hirshfeld, DFT conformational, cytotoxic, and anti-toxoplasma studies of new indole-hydrazone derivatives. *Int. J. Mol. Sci.* 24, 13251. doi:10.3390/ijms241713251
- Hikal, W. M., Tkachenko, K. G., Said-Al Ahl, H. A., Sany, H., Sabra, A. S., Baeshen, R. S., et al. (2021). Chemical composition and biological significance of thymol as antiparasitic. *Open J. Ecol.* 11, 240–266. doi:10.4236/oje.2021.113018
- Jyoti, D. D., Singh, D., Kumar, G., Karnatak, M., Chandra, S., Prakash Verma, V., et al. (2019). Thymol chemistry: a medicinal toolbox. *Curr. Bioact. Compd.* 15, 454–474. doi:10.2174/1573407214666180503120222
- Kamal, A., Bolla, N. R., Srikanth, P. S., and Srivastava, A. K. (2013). Naphthalimide derivatives with therapeutic characteristics: a patent review. *Expert Opin. Ther. Pat.* 23, 299–317. doi:10.1517/13543776.2013.746313
- Katariya, K., Soni, R., Nakum, K. J., Patel, D., Nada, S., and Hagar, M. (2024). New symmetric/unsymmetrical self-assembling salicylaldehyde-chalcones: synthesis, photophysical study and DFT approach. *J. Mol. Struct.* 1295, 136610. doi:10.1016/j.molstruc.2023.136610
- Lv, R., and Chen, Z. (2017). Thymol inhibits cell migration and invasion by downregulating the activation of PI3K/AKT and ERK pathways in human colon cancer cells. *Trop. J. Pharm. Res.* 16, 2895–2901. doi:10.4314/tjpr.v16i12.13
- Najoom, S., Fozia, F., Ahmad, I., Wahab, A., Ahmad, N., Ullah, R., et al. (2021). Effective antiplasmodial and cytotoxic activities of synthesized zinc oxide nanoparticles using *Rhazya stricta* leaf extract. *Evidence-Based Complementary Altern. Med.* 2021, 1–9. doi:10.1155/2021/5586740
- Nandi, T., and Khanna, M. (2022). Anti-viral activity of thymol against influenza A virus. *EC Microbiol.* 18, 98–103.
- Operario, D. J., Bristol, L. S., Liotta, J., Nydam, D. V., and Houpt, E. R. (2015). Correlation between diarrhea severity and oocyst count via quantitative PCR or fluorescence microscopy in experimental cryptosporidiosis in calves. *Am. J. Trop. Med. Hyg.* 92, 45–49. doi:10.4269/ajtmh.14-0488

- Politzer, P., and Murray, J. S. (2021). "Molecular electrostatic potentials: significance and applications," in *Chemical reactivity in confined systems: theory, modelling and applications*, 113–134.
- Poulose, A., and Croteau, R. (1978). Biosynthesis of aromatic monoterpenes: conversion of γ -terpinene to p-cymene and thymol in *Thymus vulgaris* L. *Archives Biochem. Biophysics* 187, 307–314. doi:10.1016/0003-9861(78)90039-5
- Qian, X., Xiao, Y., Xu, Y., Guo, X., Qian, J., and Zhu, W. (2010). "Alive" dyes as fluorescent sensors: fluorophore, mechanism, receptor and images in living cells. *Chem. Commun.* 46, 6418–6436. doi:10.1039/c0cc00686f
- Ryan, U., Zahedi, A., and Paparini, A. (2016). Cryptosporidium in humans and animals—a one health approach to prophylaxis. *Parasite Immunol.* 38, 535–547. doi:10.1111/pim.12350
- Sathe, P. S., Rajput, J. D., Gunaga, S. S., Patel, H. M., and Bendre, R. S. (2019). Synthesis, characterization, and antioxidant activity of thymol-based paracetamol analogues. *Res. Chem. Intermed.* 45, 5487–5498. doi:10.1007/s11164-019-03914-0
- Sennouni, C. I., Oukouia, M., Jabeur, I., Hamdani, H., Chami, F., and Remmal, A. (2022). *In vitro* and *in vivo* study of the antiparasitic effect of thymol on poultry drinking water. *Acta Sci. Biol. Sci.* 44, e58571. doi:10.4025/actascibiolsci.v44i1.58571
- Singh, A. K., Rajendran, V., Pant, A., Ghosh, P. C., Singh, N., Latha, N., et al. (2015). Design, synthesis and biological evaluation of functionalized phthalimides: a new class of antimalarials and inhibitors of falcipain-2, a major hemoglobinase of malaria parasite. *Bioorg. & Med. Chem.* 23, 1817–1827. doi:10.1016/j.bmc.2015.02.029
- Soni, R., Nakum, K. J., Katariya, K. D., Gergis, M., Hagar, M., and Sharma, V. S. (2024). Biphenyls embedded Schiff base-bis esters: self-assembling behaviour, impact of additional aromatic ring and ester linkage and their DFT investigations. *Liq. Cryst.* 51, 1215–1229. doi:10.1080/02678292.2024.2350044
- Staneva, D., Vasileva-Tonkova, E., and Grabchev, I. (2019). A new bioactive complex between Zn (II) and a fluorescent symmetrical benzanthrone tripod for an antibacterial textile. *Materials* 12, 3473. doi:10.3390/ma12213473
- Tanaka, K. (2024). New strategy for lowering the energy levels of one frontier molecular orbital in conjugated molecules and polymers based on Aza-substitution at the isolated HOMO or LUMO. *Polym. J.* 56, 61–70. doi:10.1038/s41428-023-00843-z
- Wang, Z.-D., Liu, Q., Liu, H.-H., Li, S., Zhang, L., Zhao, Y.-K., et al. (2018). Prevalence of Cryptosporidium, microsporidia and Isospora infection in HIV-infected people: a global systematic review and meta-analysis. *Parasites & vectors* 11, 28–19. doi:10.1186/s13071-017-2558-x